SUBMITTED TO ApJ
Preprint typeset using LaTeX style emulateapj v. 12/16/11

arXiv:1703.08301v1 [astro-ph.CO] 24 Mar 2017

HALO NONLINEAR RECONSTRUCTION

Yu Yu[1,*], Hong-Ming Zhu[2,3], and Ue-Li Pen[4,5,6,7]

submitted to ApJ

ABSTRACT

We apply the nonlinear reconstruction method (Zhu *et al.*, arXiv:1611.09638) to simulated halo fields. For halo number density 2.77×10^{-2} $(h^{-1}\mathrm{Mpc})^{-3}$ at $z = 0$, corresponding to the SDSS main sample density, we find the scale where the noise saturates the linear signal is improved to $k \gtrsim 0.36$ $h\mathrm{Mpc}^{-1}$, a factor of 2.29 improvement in scale, or 12 in number of linear modes. The improvement is less for higher redshift or lower halo density. We expect this to substantially improve the BAO accuracy of dense, low redshift surveys, including the SDSS main sample, 6dFGS and 21cm intensity mapping initiatives.

Keywords: cosmology: large-scale structure of universe

1. INTRODUCTION

Measuring the expansion history and structure growth has been a major focus of modern observational cosmology. A lot of information about our Universe is being decoded from the current surveys, like BOSS (Alam et al. (2016)), 6dFGS (Jones et al. (2009)), and etc. Ambitious on-going and future surveys, like eBOSS[9], DESI (DESI Collaboration et al. (2016)), PFS (Takada et al. (2014)), CHIME (Bandura et al. (2014)), HIRAX (Newburgh et al. (2016)), BINGO (Battye et al. (2016)), Tianlai[10], HETDEX[11], Euclid[12], WFIRST[13], and etc, will further extend the exploration in both width and depth. These surveys are expected to bring us significant improvement in the understanding of our Universe.

Most of the future surveys are aiming at the high redshift universe. These surveys will observe matter distributions with less nonlinear evolution in a huge cosmic volume. However, only very bright objects/features could be detected in these surveys. On the contrary, the low redshift universe is relatively easy to observe, but suffers from significant nonlinear effects and limited volume. The late-time nonlinear evolution is a complicated process and the statistics is difficult to model. This induces systematics in the statstics of cosmic probes (e.g., the broadening and shifting of the baryon accoustic oscillation (BAO) peak in galaxy 2-point correlation function). It also prevents a simple mapping from the final state to the initial conditions that are predicted by theories. As a result, a large portion of the cosmic information is encoded into complicated high-order statistics, and even worse, some of them is lost (e.g., Rimes & Hamilton (2005, 2006); Neyrinck et al. (2006); Carron & Neyrinck (2012)).

A part of the information loss could be recovered by a process known as "reconstruction" (e.g., Eisenstein et al. (2007)). The nonlinear density field is smoothed on the linear scale (~ 10 $h^{-1}\mathrm{Mpc}$) to make the Zel'dovich approximation valid. The linear displacement is estimated and used to move the galaxies back and to move a random sample in the same way. These two new fields form the reconstructed density field, which has a sharper BAO peak, leading to more stringent cosmological parameter constraints. In the literatures, this reconstruction method was theoretically understood and modeled (e.g., Padmanabhan et al. (2009), Noh et al. (2009), White (2015), Seo et al. (2016)), tested against numerical simulations (e.g., Seo et al. (2008), Seo et al. (2010), Mehta et al. (2011), Achitouv & Blake (2015), Schmittfull et al. (2015), Obuljen et al. (2016)), and applied on observations (e.g., Padmanabhan et al. (2012), Xu et al. (2013), Anderson et al. (2014), Kazin et al. (2014), Ross et al. (2015), Beutler et al. (2016), Hinton et al. (2017), Beutler et al. (2017)) extensively.

Zhu et al. (2016b) presented a direct approach to nonparametrically reconstruct the linear density field, by solving for a unique displacement potential consistent with the nonlinear density map and positive definite coordinate transformation. Different from Eisenstein et al. (2007), the reconstructed (nonlinear) displacement is not used to move the galaxy positions. Instead, the reconstructed density field is directly derived by the negative divergence of the reconstructed displacement. Hereafter, we call this reconstruction process as *nonlinear reconstruction*. Using the simulated dark matter density field, Zhu et al. (2016b) found that the reconstructed density

[1] Key Laboratory for Research in Galaxies and Cosmology, Shanghai Astronomical Observatory, Chinese Academy of Sciences, 80 Nandan Road, Shanghai, 200030, China
[*] yuyu22@shao.ac.cn
[2] Key Laboratory for Computational Astrophysics, National Astronomical Observatories, Chinese Academy of Sciences, 20A Datun Road, Beijing 100012, China
[3] University of Chinese Academy of Sciences, Beijing 100049, China
[4] Canadian Institute for Theoretical Astrophysics, University of Toronto, 60 St. George Street, Toronto, Ontario M5S 3H8, Canada
[5] Dunlap Institute for Astronomy and Astrophysics, University of Toronto, 50 St. George Street, Toronto, Ontario M5S 3H4, Canada
[6] Canadian Institute for Advanced Research, CIFAR Program in Gravitation and Cosmology, Toronto, Ontario M5G 1Z8, Canada
[7] Perimeter Institute for Theoretical Physics, 31 Caroline Street North, Waterloo, Ontario, N2L 2Y5, Canada
[9] eBOSS, http://www.sdss.org/surveys/eboss/
[10] Tianlai, http://tianlai.bao.ac.cn
[11] HETDEX, http://www.hetdex.org/
[12] EUCLID, http://sci.esa.int/euclid/
[13] WFIRST, http://wfirst.gsfc.nasa.gov/

field recovers the coherence with linear initial conditions up to $k \sim 1\ h\mathrm{Mpc}^{-1}$, a factor of ~ 6 improvement in scale compared to the nonlinear density field. The information content is also found to be increased by a factor of ~ 50 after the nonlinear reconstruction (see Pan et al. (2016)). Yu et al. (2016) quantified the limits of all Lagrangian reconstruction methods by measuring the correlations in Lagrangian space (i.e., the correlations between the initial displacement and final displacement) in simulation.

Nonlinear reconstruction generalizes the application of linear displacement theory to fully non-linear fields, potentially substantially expanding the BAO and redshift space distortions (RSD) information content of dense large-scale structure surveys. As shown in Zhu et al. (2016b), the noise part of the reconstructed field dominates over the linear signal at $k \gtrsim 0.6\ h\mathrm{Mpc}^{-1}$, suggesting that all BAO peaks may be recovered from the present day density field, opening up the potential of recovering cosmic information including BAO down to the Poisson noise limit. To apply this novel reconstruction method to observations, we need to consider the reconstruction from galaxy/halo density fields. This paper presents the performance test on the simulated halo fields with three number densities and three redshifts.

This article is organized as follows. In Sect. 2, we briefly introduce the reconstruction method. The performance tests on various situations are presented in Sect. 3. We summarize the result and discuss future directions in Sect. 4.

2. RECONSTRUCTION ALGORITHM

The basic idea of the reconstruction is to build a bijective curvilinear coordinate system $\boldsymbol{\xi} \equiv (\xi_1, \xi_2, \xi_3)$, where the mass per volume element is constant,

$$\rho(\boldsymbol{\xi})\mathrm{d}^3\boldsymbol{\xi} = \text{constant} \ . \tag{1}$$

We call this curvilinear coordinate system as *potential isobaric gauge/coordinates*. It becomes analogous to "synchronous gauge" and "Lagrangian coordinates" before shell crossing, but allows a unique mapping even after shell crossing. In this scenario, the mass element at final physical position $\boldsymbol{x}$ comes from the estimated initial Lagrangian position given by the potential isobaric coordinate $\boldsymbol{\xi}$. In the following, we use Latin indices to denote Cartesian coordinate labels x^i, while Greek indices to denote the curvilinear coordinates ξ^μ.

Since we attempt to follow the potential flow instead of the vorticity, we define a coordinate transformation that is a pure gradient,

$$x^i = \xi^\mu \delta^i_\mu + \Delta x^i \ , \tag{2}$$

where the displacement

$$\Delta x^i \equiv \frac{\partial \phi}{\partial \xi^\nu}\delta^{i\nu} \ . \tag{3}$$

We call ϕ as the displacement potential.

Since the displacement from the initial Lagrangian position to the final Eulerian position can be large, it's difficult to obtain the solution directly. One efficient and robust algorithm is the moving mesh approach, which is originally introduced for the adaptive particle-mesh N-body algorithm and the moving mesh hydrodynamics algorithm (See Pen (1995, 1998)). These algorithms attempt to evolve the curvilinear coordinate along with the matter/energy density field to maintain constant mass/energy-resolution. In our case, this approach solves for the displacement potential perturbatively and iteratively. The evolution of the curvilinear coordinate system is determined by a linear elliptic evolution equation

$$\partial_\mu(\rho\sqrt{g}e^\mu_i\delta^{i\nu}\partial_\nu\dot{\phi}) = \Delta\rho \ , \tag{4}$$

where $\sqrt{g} = \det(e^i_\mu)$ is the Jabobian of the transformation matrix $e^i_\mu = \partial x^i/\partial\xi^\mu$ and $\Delta\rho = \bar{\rho} - \rho\sqrt{g}$. The time derivative here is relative to the iteration step. We obtain the change of the displacement potential $\Delta\phi = \dot{\phi}\Delta t$ at each iteration step and then update the density field in the new coordinate frame. The final solution is given by

$$\phi = \Delta\phi^{(1)} + \Delta\phi^{(2)} + \Delta\phi^{(3)} + \cdots \ , \tag{5}$$

where $\Delta\phi^{(i)}$ is the result from the ith iteration. We also implement the smoothing and limiting schemes to guarantee the triad e^μ_i is positive definite at each step. The elliptic equation can be solved using the multigrid algorithm described also in Pen (1995).

The above process ensures that the coordinate transform is positive definite. The coordinate lines will not cross and the eigenvalues for this coordinate transform are always positive. For the reconstruction from the dark matter density field and in the case that dark matter particles follow a irrotational potential flow and no shell crossing happens, the reconstructed displacement is exact up to a global spatial translation. However, shell crossing happens in the nonlinear regime. This reconstruction algorithm gives an approximate solution to the true displacement.

We are aiming at reconstructing a density field with more linear information. We define the negative Laplacian of the reconstructed displacement potential as the *reconstructed density field*,

$$\delta_r(\boldsymbol{\xi}) \equiv -\nabla_{\boldsymbol{\xi}} \cdot \Delta\boldsymbol{x}(\boldsymbol{\xi}) = -\nabla^2_{\boldsymbol{\xi}}\phi \ . \tag{6}$$

See Zhu et al. (2016b) for a more detailed physical interpretation of this reconstruction process and the relation with Eisenstein et al. (2007).

n_h	2.77×10^{-2}	2.77×10^{-3}	2.77×10^{-4}	$M_{\max}$
$z=0.0$	2.15×10^{10}	1.84×10^{12}	2.10×10^{13}	2.11×10^{15}
$z=0.5$	6.44×10^{10}	1.70×10^{12}	1.53×10^{13}	1.16×10^{15}
$z=1.0$	5.58×10^{10}	1.44×10^{12}	1.05×10^{13}	6.12×10^{14}

Table 1
Detailed information for various halo samples used in the performance test. The first row indicates the sample number density, in unit of $(h^{-1}\mathrm{Mpc})^{-3}$. The minimum halo mass for three number densities and three redshifts is listed in the table, in unit of $M_\odot/h$. In the last column, the maximum halo mass is listed for three redshifts.

3. IMPLEMENTATION AND RESULT

3.1. *Halo density field*

To test the performance of the reconstruction algorithm, we use a simulation run with the CUBEP^{3}M code (see Harnois-Déraps et al. (2013)), involving 2048^3 dark matter particles in a box with side length of $600\ h^{-1}\mathrm{Mpc}$. The particle-mesh process adopts a 4096^3 grid and the

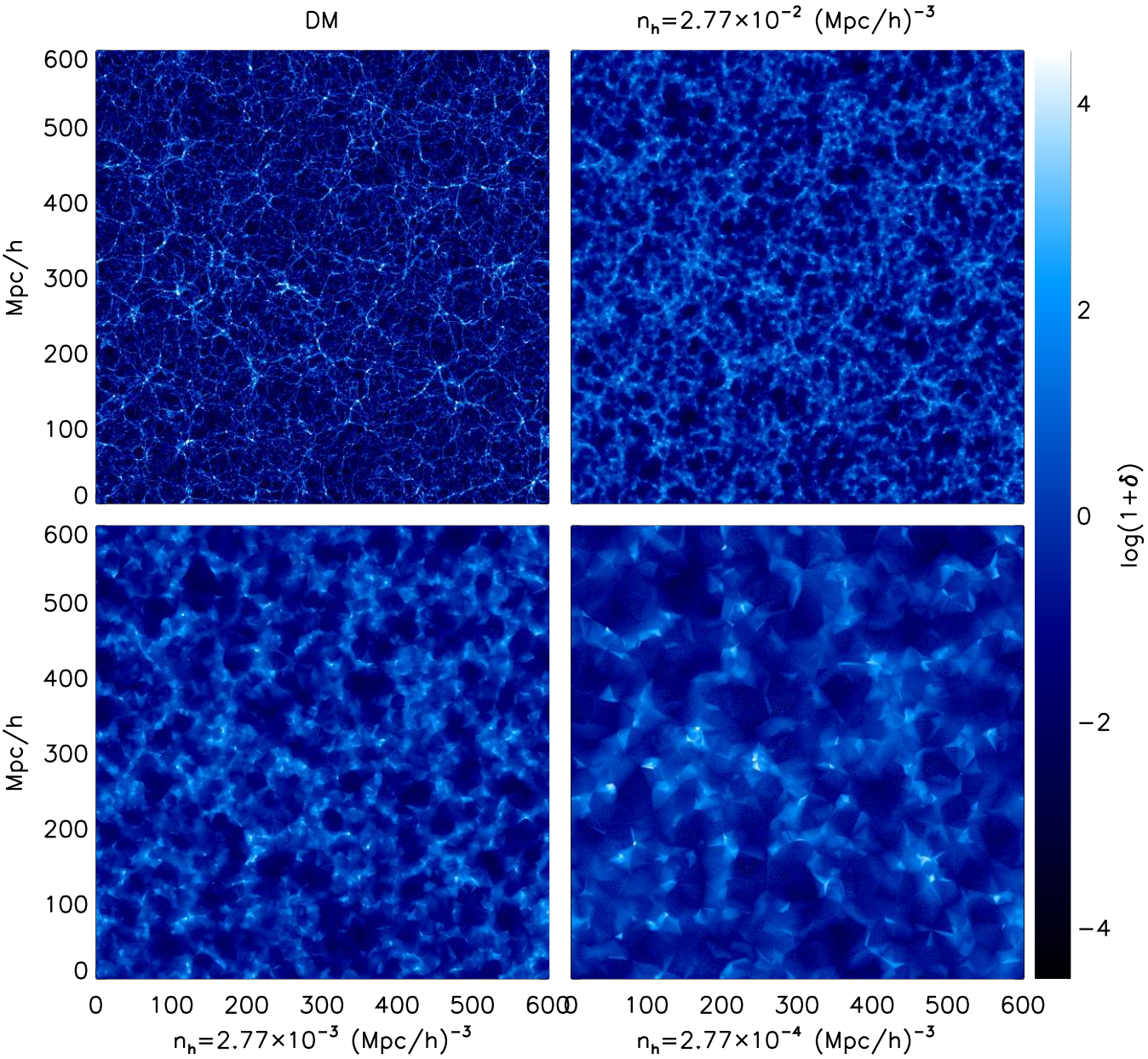

Figure 1. The input DM density field (top-left) and halo fields with number density of 2.77×10^{-2}, 2.77×10^{-3}, 2.77×10^{-4} $(h^{-1}\mathrm{Mpc})^{-3}$ for $z=0$. These halo fields are produced by DTFE method to avoid empty grid and improve the stability of the reconstruction algorithm.

particle-particle process is involved. We output the snapshot at $z=0$, 0.5, and 1 to cover the typical redshift for current and on-going galaxy surveys. The reconstruction and analysis are performed on 512^3 curvilinear and uniform grids. This grid size ensures that the following analysis is reliable and the reconstruction is not computationally expensive. We adopt a spherical overdensity halo finder. The smallest halo contains 10 particles and has a halo mass of $2.15\times10^{10}M_\odot/h$. We construct three halo samples with number density of 2.77×10^{-2}, 2.77×10^{-3}, 2.77×10^{-4} $(h^{-1}\mathrm{Mpc})^{-3}$ by setting the lower limit in halo mass. The detailed halo sample information is listed in Table 1.

The halo field is a discrete, highly non-uniform field. Traditional mass assignment methods (e.g., NGP, CIC, TSC) will leave many grids empty. As the reconstruction algorithm aims to build a potential isobaric gauge in which the mass per volume element is constant, a large area with no matter will cause the algorithm unstable. We need an appropriate mass assignment method to avoid this situation. We tried both the Voronoi and Delaunay tessellation method (Bernardeau & van de Weygaert (1996); van de Weygaert & Schaap (2009)) and finally choose to adopt the better performing De-

launay tessellation method by the DTFE code (see Cautun & van de Weygaert (2011)). It is a linear first-order version of Natrual Neighbour Interpolation. The Delaunay tessellation is constructed from the input halo catalogue and these spatial volume-covering divisions of space into mutually disjunct tetrahedral cells adapt to the local density and the local geometry of the point distribution. It represents the natural method of reconstructing from a discrete set of samples a volume-covering and continuous density field using the maximum of information contained in the point distribution. Figure 1 shows the density slice produced by the DTFE method for simulated dark matter and the corresponding three halo fields at $z = 0$. The triangular shaped color blocks observed in the bottom-right plot is a feature for such a low density sample. Next, we apply the reconstruction algorithm on these halo fields to quantify the performance.

3.2. *Number of iteration steps*

To maintain positive coordinate transform for each step, smoothing and limiting scheme is adopted during the reconstruction. This prevents reaching a final status of exactly constant mass per volume element. In practice, we use the power spectrum of the reconstructed density field and its cross-correlation coefficient with the initial condition as the convergence criteria.

Comparing results at different iteration steps, we found that we only need $\sim$ 600 steps for the reconstruction algorithm to reach convergence for these halo samples, much less than ~ 1500 steps for the reconstruction from a nonlinear dark matter density field. By observing the power spectrum of the reconstructed density field and its cross-correlation coefficient with the initial condition at different iteration steps, we found that the results reach convergence fast on large scales. For the reconstruction from a nonlinear dark matter density field, most of the computing time is spent on the reconstruction from nonlinear small scales. This reconstruction method outperforms others by taking use of these information residing in nonlinear regime (See Zhu et al. (2016b)). However, the halo field is a discrete sample, in which a part of small scale information is missing. This comes out as the fast convergence for reconstruction from halo field.

For a halo sample with lower number density, it contains less usable small scale information. The number of iteration steps to reach convergence decreases toward lower halo density. For convenience, we just fix the number of iteration steps to be 600 for all the halo samples.

3.3. *Dependence on halo number density*

In the left panel of Figure 2, we present the power spectrum for the input halo fields and the reconstructed density fields. The cross-correlation coefficients with the linear density field are presented in the right panel. As reference, we also plot the result for the reconstruction from the nonlinear dark matter density field at the top row.

Different from the method proposed by Eisenstein et al. (2007), the reconstruction process in this work is purely a mathematical approach, which does not involve any cosmological dynamics. Without the assumptions on the fiducial cosmology, galaxy bias, growth rate, and etc, the algorithm always find the potential isobaric coordinate of which each volume element has approximately constant mass. This process ensures that the reconstructed density field is same with the input field at sufficiently large scale. Halo is a biased tracer of the underlying dark matter density field. Thus, the reconstructed fields also show the same bias to linear density field at small k. The main purpose of this work is to valid the reconstruction method on the halo field, by investigating the cross-correlation with the initial conditions. The bias presented in the reconstructed field will not influence the results.

The reconstruction performance is influenced by the number density. For DM fields, the cross-correlation coefficient curve is shifted toward small scale by a factor ~ 6 by the reconstruction. We observe smaller amount of shift (less improvement) toward decreasing halo number density. For the highest density case, $n_h = 2.77 \times 10^{-2}$ $(h^{-1}\mathrm{Mpc})^{-3}$ sample, the shift is ~ 2.5. For the intermediate sample, $n_h = 2.77 \times 10^{-3}$ $(h^{-1}\mathrm{Mpc})^{-3}$, the shift is $\lesssim 2$. For the lowest density case, only a very small improvement is observed.

Similar as the analysis in Seo et al. (2016), to clearly show how much linear signal is recovered by the reconstruction process, we decompose the density field into two terms,

$$\delta(k) = C(k)\delta_L(k) + n(k) \ , \tag{7}$$

in which $C(k)\delta_L(k)$ is completely correlated with the linear density field. The pre-factor $C(k)$, often dubbed as the "propagator" (e.g., Crocce & Scoccimarro (2006, 2008); Matsubara (2008); Taruya et al. (2009)), could be obtained by

$$C(k) = \frac{P_{\delta_L\delta}(k)}{P_{\delta_L}(k)} \ . \tag{8}$$

The remaining noise term is just $n(k) = \delta(k) - C(k)\delta_L(k)$. This decomposition of the density field directly leads to the decomposition of the power spectrum into a linear signal term plus a noise term (also called "mode-coupling" term),

$$P_\delta(k) = P_s(k) + P_n(k) \ , \tag{9}$$

in which $P_s(k) = C^2(k)P_{\delta_L}(k)$ is the linear signal term. The lower limit in scale where the BAO signal could be robustly measured is quantified by the scale where the linear signal term equals the noise term.

We present the power spectrum decomposition, Equation (9), for both the input halo fields and the reconstructed fields in Figure 3. The results are scaled so that the total power $P_s(k)+P_n(k)$ equals the halo power spectrum with familiar NGP mass assignment, to better explain the results. The reconstructed field not only has larger linear signal term, but also has lower noise term than the input field. The downward arrows indicate the scale where the linear signal term equals to the noise term. We clearly see the decrease of the scale (increase in k) by the reconstruction process. The improvement reaches a factor of 2.29, 1.89 and 1.27 for $n_h = 2.77 \times 10^{-2}$, 2.77×10^{-3}, 2.77×10^{-4} $(h^{-1}\mathrm{Mpc})^{-3}$, respectively. Specifically, for the most concern case, this scale is decreased from $k = 0.16$ to 0.36 $h\mathrm{Mpc}^{-1}$.

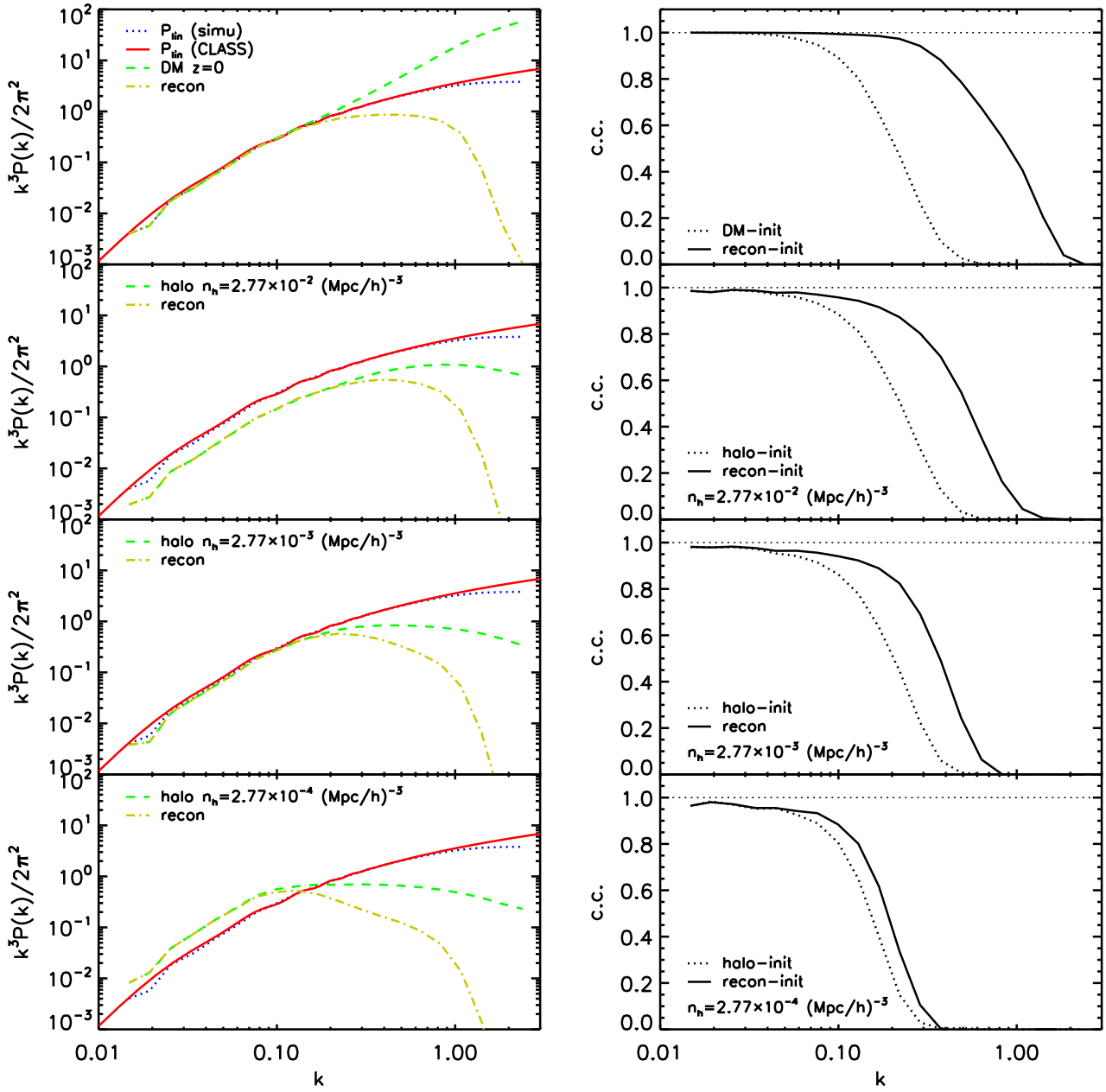

Figure 2. The left panel presents the power spectrum of the input fields and the reconstructed fields for $z = 0$. As reference, linear power spectrum from theory and simulation initial condition are also plotted. Right panel presents the cross-correlation coefficients between the reconstructed fields and linear density field in solid line. For comparison, the cross-correlation coefficients between the input fields and linear density field are plotted in dotted line. From top to bottom, the input field is DM density field, halo fields with number density of 2.77×10^{-2}, 2.77×10^{-3}, 2.77×10^{-4} $(h^{-1}\mathrm{Mpc})^{-3}$, respectively.

Note that the noise term has two contributions, one from the nonlinear clustering and another from the shot noise. We present the expected shot noise power spectrum for NGP mass assignment in Figure 3. For the highest number density case (top panel), the noise term of the input field exceeds the expected shot noise contribution a lot. This implies that the nonlinear clustering domintes over the shot noise. After the reconstruciton, linear signal is recovered and meanwhile the nonlinear clustering is suppressed. Thus, the nonlinear reconstruction is powerful for this case. For the lowest number density case (bottom panel), the noise term of the input field is dominated by the shot noise. The halo field with such a low numder density is almostly the combination of the linear signal plus the Poisson noise. In this case, there is no usable nonlinear information and the reconstruction performance is limited.

In Figure 4, we present the comparison of cross-correlation coefficient for various input and reconstructed fields, including the DM field and halo samples with $n_h = 2.77 \times 10^{-2}$ and 2.77×10^{-3} $(h^{-1}\mathrm{Mpc})^{-3}$. These three input fields have similar coherence with the initial conditions. This implies that $n_h \gtrsim 2.77 \times 10^{-3}$ $(h^{-1}\mathrm{Mpc})^{-3}$ is roughly sufficient for extracting BAO information without any reconstruction process. However, the reconstruction performance indeed benefits from high

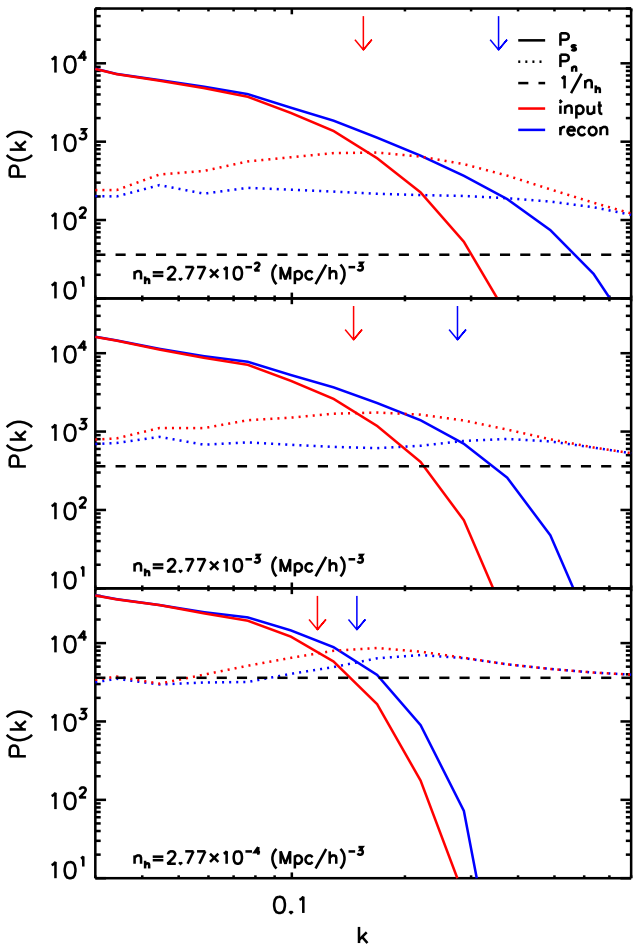

Figure 3. The power spectrum decomposition for the input (red) and reconstructed (blue) field. The linear signal term is presented in solid line, while the noise term in dotted line. All the results are scaled so that the total power equals to the halo power spectrum with familiar NGP mass assginment. The expected shot noise for NGP mass assignment, $1/n_h$, is also plotted in dashed line. From top to bottom, the input halo field has number density of 2.77×10^{-2}, 2.77×10^{-3}, 2.77×10^{-4} $(h^{-1}\mathrm{Mpc})^{-3}$, respectively. The downward arrows indicate the scale where the signal term equals the noise term.

halo number density. This strongly motivates us to go deeper for low redshift (local) surveys.

3.4. *Dependence on redshift*

We present the redshift dependence of the reconstruction performance for each halo sample in Figure 5. Note that these halo samples at different redshifts are not the same halo population at different cosmic epoch, since we just choose a specific halo number density for all three redshifts.

The top panel shows the result for the input halo sample with number density of 2.77×10^{-2} $(h^{-1}\mathrm{Mpc})^{-3}$. The higher redshift halo field experiences less nonlinear evolution, and thus contains more linear information. The reconstruction increases the cross-correlation coefficients in a similar way for all the three redshifts we investigated. The performance is only mildly degraded for $z = 1$.

For the input halo field with a number density of 2.77×10^{-3} $(h^{-1}\mathrm{Mpc})^{-3}$, we can still see the improvements for all the three redshifts. However, the improve-

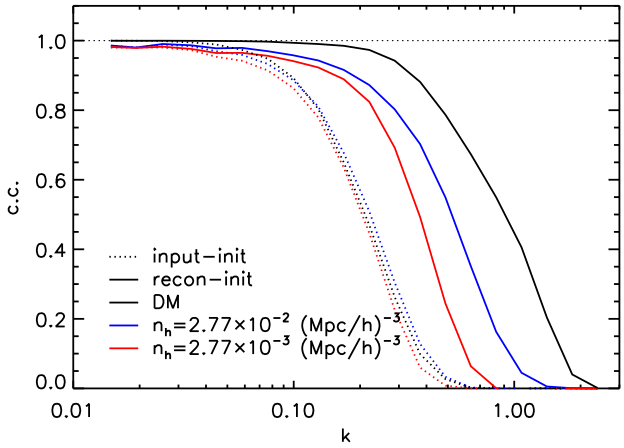

Figure 4. The comparison of cross-correlation coefficient for various input and reconstructed fields, including the DM field and two halo samples. The three input fields have similar coherence with the initial condition. But, the reconstructed fields benefits from higher number density.

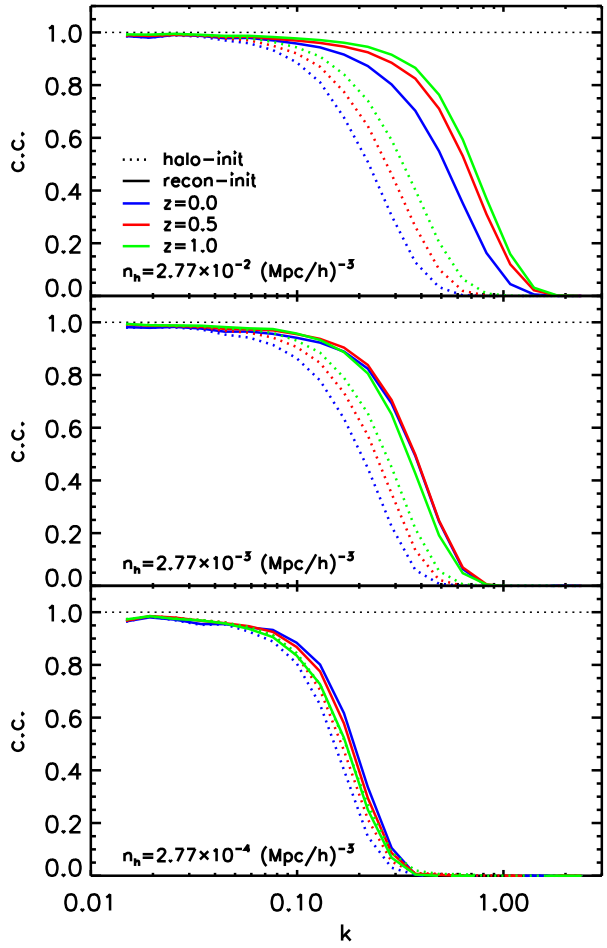

Figure 5. The cross-correlation coefficient between the reconstructed fields and the linear density field is presented in solid line. For comparison the result for the input halo fields is presented in dotted line. For a given halo number density, the result for $z = 0$, 0.5, and 1 is presented in blue, red, and green, respectively.

ment is less obvious toward higher redshift. This could be explained by the fact that the higher redshift halo field has not only a lower nonlinear clustering effect, but also a relatively larger shot noise contribution. Thus, the power of the nonlinear reconstruction is limited. As a result, the reconstruction recovers the cross-correlation to comparable level for all the three redshifts.

For the number density of 2.77×10^{-4} $(h^{-1}\mathrm{Mpc})^{-3}$ case, the input halo fields at three redshifts contain similar coherence with the initial condition. Meanwhile, the noise term of them is dominated by the large Poisson noise. After the reconstruction, we only observe very small or no improvement for these redshifts.

In the two lowest density case, we observe the convergence for the recovered cross-correlation coefficients for different redshifts. If we define a characteristic scale to quantify the performance, namely where the cross-correlation coefficients drops to 0.7 (corresponds to $S/N = 1$ for the power spectrum decomposition Equation (9), see Zhu et al. (2016a)), we find this roughly scales as $n_h^{1/3}$. This also implies that the reconstruction performance is already limited by Poisson noise for a given halo number density. It is also this limitation that mildly degrades the reconstruction performance for $n_h = 2.77 \times 10^{-2}$ $(h^{-1}\mathrm{Mpc})^{-3}$ at $z = 1$.

4. CONCLUSION AND DISCUSSION

We tested the reconstruction method proposed in Zhu et al. (2016b) on the simulated halo fields with three different number densities and at three redshifts. The reconstruction performance is quantified by the extension in scale where the BAO signal could be robustly measured. We decomposed the power spectrum of both the input field and the reconstructed field into a linear signal term plus a noise term. This scale is defined at where the linear term equals the noise term. For the most concerned case, $n_h = 2.77 \times 10^{-2}$ $(h^{-1}\mathrm{Mpc})^{-3}$ at $z = 0$, which is close to the condition of SDSS main galaxy sample, we found the improvement reaches a factor of 2.29 in scale (from $k = 0.16$ to 0.36 $h\mathrm{Mpc}^{-1}$), or equivalently, a factor of 12 for available modes for BAO measurement.

The reconstruction performance depends on the halo number density. At $z = 0$, the improvements reach a factor of 2.29, 1.69 and 1.15 for halo sample with number density of $n_h = 2.77 \times 10^{-2}$, 2.77×10^{-3}, 2.77×10^{-4} $(h^{-1}\mathrm{Mpc})^{-3}$, respectively. We also reported the limited reconstruction power for the low number density cases, which roughly correspond to the targets of the on-going high redshift surveys.

To apply the new reconstruction method on discrete halo fields, we need a suitable mass assignment method, which does not induce extra degree-of-freedom in the process. The DTFE method we adopted in this work is a straightforward attempt. We also tried other methods like the Voronoi tessellation. The performance is a little bit downgraded by adopting the Voronoi tessellation method. There may exist better mass-assignment worth a try in dealing with this issue. However, for the most concerned high density case, the choice of mass assignment is less important. For low density case, none of the mass assignment could present the underlying DM field well without introducing extra parameters.

As discussed in Zhu et al. (2016b), the Lagrangian BAO reconstruction algorithm involves displacing individual objects according to the linear displacement that is computed from the observed galaxy distribution under certain model assumptions (the smoothing scale, galaxy bias, growth rate, etc (See Eisenstein et al. (2007)). The results depend on the assumed fiducial model and must be tested against different parameter choices, which is computationally expensive (See Padmanabhan et al. (2012)). The reconstruction method used in this work is a purely mathematical approach with no cosmological dynamics involved.

The reconstruction from the nonlinear DM field gives an estimate for displacement field (See Zhu et al. (2016b)). This is not the case for the reconstruction from a biased tracer, i.e. the halo field. The reconstructed displacement from a biased halo sample does not responds to the halo displacement in the Lagrangian halo formation scenario. However, one could involve the above mentioned model assumptions (the fiducial cosmology, galaxy bias, growth rate, etc) to correct the bias and RSD effect prior to the reconstruction process. In this way, the reconstructed displacement field is more physically motivated and might have further applications. We leave this to future investigation.

We focused on investigating the dependence on the halo number density and redshift. One immediate and urgent future work is the performance test on the halo samples with the RSD effect. The RSD effect is due to the structure growth, and thus contains important cosmological information. The observed position of an object is shifted by its peculiar velocity along the line-of-sight. This simply adds an extra offset on the real displacement field. Thus, the displacement field reconstructed from the observed density field automatically includes this additive offset. Since much less nonlinearities involved in the displacement potential, the measurement and modeling of RSD will be improved significantly. This also helps to simultaneously model the BAO and RSD signal.

To apply the proposed reconstruction method in observations, there are many observational issues need investigation, including the selection function, the survey geometry, and etc. We will investigate these issues in near future.

ACKNOWLEDGMENT

We thank Pengjie Zhang, Xin Wang, Xuelei Chen, Kwan Chuen Chan, Haoran Yu, Morgan Bennett and Qiaoyin Pan for useful discussions. This work was supported by the national science foundation of China (Grant No. 11403071). The simulation is performed on the BGQ super-computer at the SciNet HPC Consortium. SciNet is funded by the Canada Foundation for Innovation under the auspices of Compute Canada, the Government of Ontario, the Ontario Research Fund Research Excellence, and the University of Toronto. The Dunlap Institute is funded through an endowment established by the David Dunlap family and the University of Toronto. Research at the Perimeter Institute is supported by the Government of Canada through Industry Canada and by the Province of Ontario through the Ministry of Research & Innovation.

REFERENCES

Achitouv, I., & Blake, C. 2015, PRD , 92, 083523
Alam, S., Ata, M., Bailey, S., et al. 2016, ArXiv e-prints, arXiv:1607.03155
Anderson, L., Aubourg, É., Bailey, S., et al. 2014, MNRAS , 441, 24
Bandura, K., Addison, G. E., Amiri, M., et al. 2014, in Proc. SPIE, Vol. 9145, Ground-based and Airborne Telescopes V, 914522
Battye, R., Browne, I., Chen, T., et al. 2016, ArXiv e-prints, arXiv:1610.06826
Bernardeau, F., & van de Weygaert, R. 1996, MNRAS , 279, 693
Beutler, F., Blake, C., Koda, J., et al. 2016, MNRAS , 455, 3230
Beutler, F., Seo, H.-J., Ross, A. J., et al. 2017, MNRAS , 464, 3409
Carron, J., & Neyrinck, M. C. 2012, ApJ , 750, 28
Cautun, M. C., & van de Weygaert, R. 2011, The DTFE public software: The Delaunay Tessellation Field Estimator code, Astrophysics Source Code Library, arXiv:1105.0370
Crocce, M., & Scoccimarro, R. 2006, PRD , 73, 063520
—. 2008, PRD , 77, 023533
DESI Collaboration, Aghamousa, A., Aguilar, J., et al. 2016, ArXiv e-prints, arXiv:1611.00036
Eisenstein, D. J., Seo, H.-J., Sirko, E., & Spergel, D. N. 2007, ApJ , 664, 675
Harnois-Déraps, J., Pen, U.-L., Iliev, I. T., et al. 2013, MNRAS , 436, 540
Hinton, S. R., Kazin, E., Davis, T. M., et al. 2017, MNRAS , 464, 4807
Jones, D. H., Read, M. A., Saunders, W., et al. 2009, MNRAS , 399, 683
Kazin, E. A., Koda, J., Blake, C., et al. 2014, MNRAS , 441, 3524
Matsubara, T. 2008, PRD , 77, 063530
Mehta, K. T., Seo, H.-J., Eckel, J., et al. 2011, ApJ , 734, 94
Newburgh, L. B., Bandura, K., Bucher, M. A., et al. 2016, in Proc. SPIE, Vol. 9906, Society of Photo-Optical Instrumentation Engineers (SPIE) Conference Series, 99065X
Neyrinck, M. C., Szapudi, I., & Rimes, C. D. 2006, MNRAS , 370, L66
Noh, Y., White, M., & Padmanabhan, N. 2009, PRD , 80, 123501
Obuljen, A., Villaescusa-Navarro, F., Castorina, E., & Viel, M. 2016, ArXiv e-prints, arXiv:1610.05768
Padmanabhan, N., White, M., & Cohn, J. D. 2009, PRD , 79, 063523
Padmanabhan, N., Xu, X., Eisenstein, D. J., et al. 2012, MNRAS , 427, 2132
Pan, Q., Pen, U.-L., Inman, D., & Yu, H.-R. 2016, ArXiv e-prints, arXiv:1611.10013
Pen, U.-L. 1995, ApJS , 100, 269
—. 1998, ApJS , 115, 19
Rimes, C. D., & Hamilton, A. J. S. 2005, MNRAS , 360, L82
—. 2006, MNRAS , 371, 1205
Ross, A. J., Samushia, L., Howlett, C., et al. 2015, MNRAS , 449, 835
Schmittfull, M., Feng, Y., Beutler, F., Sherwin, B., & Chu, M. Y. 2015, PRD , 92, 123522
Seo, H.-J., Beutler, F., Ross, A. J., & Saito, S. 2016, MNRAS , 460, 2453
Seo, H.-J., Siegel, E. R., Eisenstein, D. J., & White, M. 2008, ApJ , 686, 13
Seo, H.-J., Eckel, J., Eisenstein, D. J., et al. 2010, ApJ , 720, 1650
Takada, M., Ellis, R. S., Chiba, M., et al. 2014, PASJ , 66, R1
Taruya, A., Nishimichi, T., Saito, S., & Hiramatsu, T. 2009, PRD , 80, 123503
van de Weygaert, R., & Schaap, W. 2009, in Lecture Notes in Physics, Berlin Springer Verlag, Vol. 665, Data Analysis in Cosmology, ed. V. J. Martínez, E. Saar, E. Martínez-González, & M.-J. Pons-Bordería, 291–413
White, M. 2015, MNRAS , 450, 3822
Xu, X., Cuesta, A. J., Padmanabhan, N., Eisenstein, D. J., & McBride, C. K. 2013, MNRAS , 431, 2834
Yu, H.-R., Pen, U.-L., & Zhu, H.-M. 2016, ArXiv e-prints, arXiv:1610.07112
Zhu, H.-M., Pen, U.-L., & Chen, X. 2016a, ArXiv e-prints, arXiv:1609.07041
Zhu, H.-M., Yu, Y., Pen, U.-L., Chen, X., & Yu, H.-R. 2016b, ArXiv e-prints, arXiv:1611.09638